# Eulerian Finite-strain Elasticity with Phase-field and the Reference Map Technique

# Farshad Ghanbari, Christian Peco

#### 1 Introduction

Many problems in science and engineering involve moving boundaries. Some well-known examples include fluid-structure interaction<sup>[1]</sup>, dendritic solidification<sup>[2]</sup>, and crack propagation<sup>[3]</sup>. Numerical treatment of such problems requires solving partial differential equations (PDEs) on moving domains with boundary conditions on unknown and moving sharp interfaces, which poses a considerable challenge<sup>[4, 5]</sup>. Phase-field modeling has gained popularity within the computational mechanics community as a powerful tool to address the difficulties associated with solving interface problems. Phase-field methods are based on reformulating the moving boundary problem using a continuous, smooth scalar variable that ranges between two

# 筆者紹介



Farshad Ghanbari is a Ph.D. candidate in the Engineering Science and Mechanics Department at Penn State. He is a member of the Biomachinery and Nanomaterials Laboratory, where he works on numerical modeling of multiphysics problems under the guidance of Dr. Christian Peco. Mr. Ghanbari received his bachelor's degree in Civil and Environmental Engineering from the

Azad University in Iran and obtained his master's degree in Civil Engineering from the University of Colorado Boulder, Colorado, USA. Mr. Ghanbari's research is focused on the phase-field modeling of constrained biological networks inspired by fungi and slime molds. He has also been involved in the development of a numerical framework for modeling the ultrasonic wave propagation in reinforced polycrystalline ice. Mr. Ghanbari's other research interests and future path include phase-field modeling of environmentally assisted fracture in material's microstructure as well as the physics informed neural networks.



Christian Peco is an Assistant Professor in the Engineering Science and Mechanics Department at Penn State, USA. Prior to his current position, Dr. Peco got his Ph.D. at Universitat Politecnica de Catalunya - Barcelona Tech and completed a postdoc at Duke University. He has collaborated with the Okinawa Institute of Science and Technology in Japan and the Idaho National Lab in USA.

Dr. Peco's research goal is to understand the nature of complex soft materials and devise pathways to apply these new material paradigms to technology. Prof. Peco's group produces original computational models, amenable to supercomputing, that allow exploring previously inaccessible physics. In combination with experiments, his group identifies novel principles and elaborate design guidelines (e.g., bio-inspired, active soft materials). Prof. Peco's trajectory includes phase-field modeling of emergence in slime molds and fungi, Eulerian elasticity, fluid-structure interaction, biomembranes, flexoelectricity, and fracture mechanics in colloidal particle rafts, a work that was selected as cover in the Soft Matter Journal.

values associated to the phases in the problem (e.g., 0 in one side of the interface and 1 in the other). The smooth variation of the scalar field, known as the phase-field variable or order parameter, effectively replaces the sharp interface with a diffuse transition zone and defines a scalar PDE over the whole domain (see Fig. 1)<sup>[6]</sup>. In consequence, the sharp interface does not have to be tracked anymore and emerges naturally from the transition from one phase to the other, given by the scalar field solution of the new PDE.

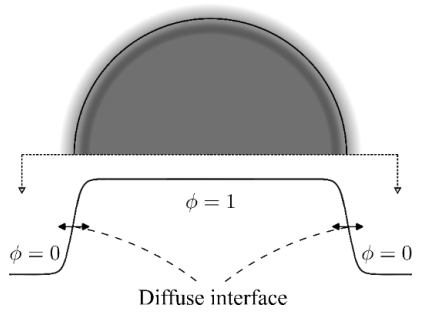


Fig. 1 Sketch of a two-phase domain marked by the scalar phase-field variable  $\varphi$ . The value of the  $\varphi$  for the outer and inner phase is zero and one, respectively. The transition between the two phases happens smoothly over the diffuse interface.

In recent years, the phase-field method has been used to model interface problems in soft matter, such as biomembrane<sup>[7, 8]</sup> and fracture mechanics<sup>[9-11]</sup>, avascular and vascular tumor growth<sup>[12, 13]</sup>, embryonic development<sup>[14]</sup>, and interactive biological networks<sup>[15]</sup>.

From the continuum mechanics point of view, the motion of a deformable body can be described using two different frameworks: the Lagrangian framework and the Eulerian framework. Engineers and scientists use the Lagrangian framework to simulate the deformation of solids, due to a reference framework and the explicit tracking of material particle motion. However, this feature can lead to severe mesh distortions when the Lagrangian approach is employed in simulations involving large deformations. Such large deformations are inherent in various applications, specifically those that involve fluid-structure interactions and soft biological materials. A suitable alternative is to use a Eulerian framework, common in fluid mechanics, which uses a fixed grid and does not explicitly track the motion of the particles. The conversion is far from trivial due to the loss of the reference configuration, which is fundamental in the constitutive equations of solids, with the elastic behavior being a prominent example. Different approaches have been proposed to activate Eulerian framework's advantages in the description of solid and fluid interface problems. One method that aims to benefit from the advantages of both Lagrangian and pure Eulerian descriptions is the Arbitrary Lagrangian-Eulerian (ALE) formulation<sup>[16]</sup>. The ALE method optimizes the shape of the mesh elements by allowing for the arbitrary movement of the mesh inside the domain while tying the boundary and interface meshes to the material points. Nevertheless, ALE is a mesh conforming method, and the development of the solid mesh interface is not straightforward. Moreover, depending on the severity of the deformations, remeshing of the domain may still be required. A reasonable strategy is to use fully Eulerian framework approaches, which are nonconforming, and thus eliminate the remeshing problem and are amenable to large scale simulations. However, these methods must elaborate formulations to correctly estimate the stress state of the solid portions of the domain due to the lack of a reference framework. A conventional approach is the advection of the strain and stress tensors over time, which typically leads to numerical dissipation and inaccuracies close to the interface. A Eulerian finite volume formulation that uses Lagrangian marker particles to compute the solid constitutive behavior has been recently presented<sup>[17]</sup>. An alternative to the advection of the conventional tensors is to use a fully Eulerian technique called the reference map technique (RMT). This methodology was introduced and developed in [18] to address the difficulties associated with conventional Eulerian solid mechanics. The RMT defines an Eulerian mapping from the deformed configuration to the reference configuration (see Fig. 2). The evolution of this reference map field is then calculated by setting its Eulerian material time derivative equal to zero. The reference map's evolution equation is supplemented with the specific initial condition defined in the next section. The equations of RMT imply that the reference map tracks the material points back to the reference configuration during the deformation, enabling us to accurately recover the deformation gradient tensor and, as a result, calculate the solid deformations without approximations. The RMT proves to be especially effective in fluid-structure interaction problems by allowing one or more deformable bodies to interact with themselves and the background fluid<sup>[19]</sup>.

On the numerical side, the RMT has been mostly implemented using the finite differences for solving the PDEs, and a level set approach to distinguish the phases (i.e., solid and fluid) of the domain. Both the volume conservation for finite difference schemes and the lack of physics associated to the interface in level set methods present substantial obstacles to its implementation in engineering schemes. As a response, several efforts have been recently put into combining the simplicity of the RMT with other numerical schemes that improve on the approximation

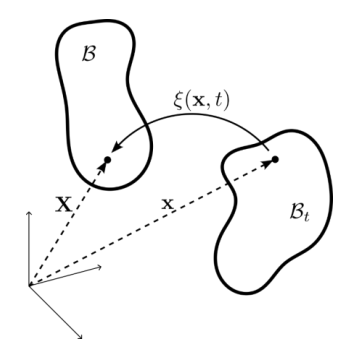


Fig. 2 A material point is mapped from the deformed configuration  $B_t$  to the reference configuration B via the reference map  $\xi(\mathbf{x},t)$ . Position vectors  $\mathbf{X}$  and  $\mathbf{x}$  mark the location of the material point, relative to the coordinate system, in the reference and the deformed configurations, respectively.

scheme and the interface treatment. For example, a combination of RMT with a finite volume-based method is presented in [20]. In this study, we present a novel approach to integrate the RMT in large deformation Eulerian elasticity with a phase-field based interface treatment, and we solve it with a finite element method (FEM) approximation. The structure of this paper is as follows: in Section 2, we define the governing equations that include the reference map's evolution equations, the phase-field modified balance of mass and balance of linear momentum, and the derivation of the weak forms needed for the FEM implementation. We then dedicate Section 3 to numerical examples that illustrate the performance of our formulation. We give our concluding remarks and future lines of work in Section 4.

#### 2 Governing Equations

We start by defining an Eulerian vector field called the reference map  $\xi(\mathbf{x}, t)$ , which initial state coincides with the reference configuration of a domain  $\Omega$ . The evolution of  $\xi(\mathbf{x}, t)$  is defined as:

$$\frac{\partial \xi(\mathbf{x},t)}{\partial t} + (\nabla \xi)\mathbf{v} = \mathbf{0},\tag{1}$$

$$\left. \left. \xi \left( \mathbf{x}, t \right) \right|_{t=0} = \mathbf{x} = \mathbf{X}, \tag{2}$$

where  $\mathbf{x}$  and  $\mathbf{X}$  indicate the location of a material point in the current and in the reference configuration, respectively.

Equation (1) along with the initial condition defined in Eq. (2) imply that the reference map  $\xi(\mathbf{x}, t)$  never changes due to the velocity field, therefore,  $\xi(\mathbf{x}, t)$  points to the location from which the material point currently at  $\mathbf{x}$  originally started. Furthermore, for a line element in the reference configuration we can write:

$$d\mathbf{X} = (\nabla \xi) \, d\mathbf{x},\tag{3}$$

therefore,

$$\mathbf{F} = (\nabla \xi)^{-1},\tag{4}$$

where  $\nabla$  here indicates the gradient with respect to the current configuration, and F is the deformation gradient tensor.

We then use the phase field  $\phi$  to indicate the solid region ( $\phi$  = 1) and the region outside the solid ( $\phi$  = 0). The evolution of

4016 特集

the phase-field is as follows:

$$\frac{\partial \phi}{\partial t} + \nabla \phi \cdot \mathbf{v} = -L \frac{\partial \Psi (\phi, \nabla \phi)}{\delta \phi},\tag{5}$$

where  $\mathbf{v}$  is the velocity field vector and L is the mobility. Moreover,  $\Psi$  is the phase-field free energy functional which we define as:

$$\Psi(\phi, \nabla \phi) = \int_{\Omega} (I + W) \, \mathrm{d}\Omega, \tag{6}$$

$$I = \frac{1}{2} \epsilon^2 |\nabla \phi|^2,\tag{7}$$

$$W = \phi^2 (1 - \phi)^2. (8)$$

In Eqs. (6) to (8), I corresponds to the interfacial energy and W is a symmetric double-well. Also,  $\epsilon$  is a small length scale proportional to the width of the diffuse interface. Taking the first variation of the free energy potential  $\Psi$  with respect to the phase field  $\phi$  yields:

$$\frac{\delta\Psi\left(\phi,\nabla\phi\right)}{\delta\phi} = \phi\left(4\phi^2 - 6\phi + 2\right) - \epsilon^2\Delta\phi,\tag{9}$$

where  $\Delta$  indicates the Laplacian operator. Therefore, Eq. (5) can be re-written as:

$$\frac{\partial \phi}{\partial t} + \nabla \phi \cdot \mathbf{v} = L \left[ \epsilon^2 \Delta \phi - \phi \left( 4\phi^2 - 6\phi + 2 \right) \right]. \tag{10}$$

We then write the phase field modified balance of mass and the balance of linear momentum in the Eulerian framework as:

$$H(\phi)\rho - J^{-1}\rho_0 = 0, (11)$$

$$\nabla \cdot (H(\phi)\sigma) + H(\phi)\rho \mathbf{b} = \rho \left[ \frac{\partial \mathbf{v}}{\partial t} + H(\phi)(\nabla \mathbf{v})\mathbf{v} \right], \quad (12)$$

where  $\rho$  and  $\rho_0$  are the current and the initial mass densities, and  $\sigma$  is the Cauchy stress.  $H(\phi)$  is a smooth Heaviside function of the phase field that localizes the mass density and the stress for the solid and is defined as:

$$H(\phi) = \frac{1}{2} \left[ \tanh\left(\frac{\phi - a}{h}\right) + 1 \right],\tag{13}$$

where a and b are constants that control the transition point and the slope of the transition zone, respectively. One can observe that the values of Eq. (13) vary between 0 and 1 for all the values of phase-field  $\phi$ . Moreover,  $\nabla$ · in Eq. (12) indicates the divergence calculated with respect to the current configuration. Also, indicating the determinant of a tensor  $\mathbf{A}$  with det $\mathbf{A}$ , we define J as:

$$J = \det \mathbf{F} = \det \left[ (\nabla \xi)^{-1} \right]. \tag{14}$$

Since the deformation gradient tensor  $\mathbf{F}$  can be described using the reference map  $\xi(\mathbf{x}t)$ , we are able to model the constitutive response of the large-deformation, thermodynamically consistent solid laws in the Eulerian framework<sup>[21]</sup>. For this study, we choose the constitutive model to be a compressible neo-Hookean elastic solid, in which the Cauchy stress  $\sigma$  is defined as:

$$\sigma = GJ^{-5/3} \operatorname{dev}(\mathbf{B}) + \kappa (J - 1) \mathbf{I}. \tag{15}$$
In Eq. (15),  $G$  and  $\kappa$  are material properties,  $\operatorname{dev}(\mathbf{B})$  is the

deviatoric part of B , the left Cauchy-Green deformation tensor, and  $\,I\,$  is the second-order identity tensor. Note that the left Cauchy-Green deformation tensor  $B\,$  can be written in terms of  $\,{\cal E}\,$  as follows:

$$\mathbf{B} = \mathbf{F}\mathbf{F}^{\mathsf{T}} = (\nabla \xi)^{-1} (\nabla \xi)^{-\mathsf{T}}.$$
 (16)

To construct the weak from, we define the space of trial solutions as:

$$U = \left\{ \phi, \rho \in H^1(\Omega) \mid \phi = \phi_g \text{ on } \partial \Omega_D \right\}, \tag{17}$$

$$S = \left\{ \mathbf{v}, \xi \in H^{1}(\Omega) \mid \mathbf{v} = \mathbf{v}_{g} \text{ on } \partial \Omega_{D} \right\}, \tag{18}$$

and the space of test functions as:

$$V = \left\{ w_{\phi}, w_{\rho} \in H^{1}(\Omega) \mid w_{\phi} = 0 \text{ on } \partial \Omega_{D} \right\}, \tag{19}$$

$$W = \left\{ \mathbf{w}_{\mathbf{v}}, \mathbf{w}_{\varepsilon} \in H^{1}(\Omega) \mid \mathbf{w}_{\mathbf{v}} = \mathbf{0} \text{ on } \partial \Omega_{D} \right\}, \tag{20}$$

where  $\partial\Omega_D$  is the Dirichlet boundary. Then the weak form becomes: Given  $\phi_g$  and  $\mathbf{v}_g$ , find  $\phi$ ,  $\rho \in U$  and  $\mathbf{v}$ ,  $\xi \in S$ , such that for all  $w_{\phi}$ ,  $w_{\rho} \in V$  and for all  $\mathbf{w}_{\mathbf{v}}$ ,  $\mathbf{w}_{\xi} \in W$ :

$$\int_{\Omega} w_{\phi} \left( \frac{\partial \phi}{\partial t} + \nabla \phi \cdot \mathbf{v} \right) d\Omega = L \epsilon^{2} \int_{\Omega} \nabla w_{\phi} \cdot \nabla \phi \, d\Omega$$

$$-L \epsilon^{2} \int_{\Omega} w_{\phi} \left( 4\phi^{2} - 6\phi + 2 \right) \phi \, d\Omega,$$
(21)

$$\int_{\Omega} w_{\rho} H(\phi) \rho d\Omega - \int_{\Omega} w_{\rho} J^{-1} \rho_0 d\Omega = 0, \tag{22}$$

$$\int_{\Omega} \rho \left[ \frac{\partial \mathbf{v}}{\partial t} + H(\phi) (\nabla \mathbf{v}) \mathbf{v} \right] \cdot \mathbf{w}_{\mathbf{v}} d\Omega$$

$$= \int_{\Omega} H(\phi) \sigma : \nabla \mathbf{w}_{\mathbf{v}} d\Omega + \int_{\Omega} H(\phi) \rho \mathbf{b} \cdot \mathbf{w}_{\mathbf{v}} d\Omega,$$
(23)

$$\int_{\Omega} \partial_t \xi \cdot \mathbf{w}_{\xi} \, d\Omega + \int_{\Omega} (\nabla \xi) \, \mathbf{v} \cdot \mathbf{w}_{\xi} \, d\Omega = 0, \tag{24}$$

with

$$\sigma = GJ^{-5/3}dev\left[(\nabla \xi)^{-1}(\nabla \xi)^{-\top}\right] + \kappa(J-1)\mathbf{I},\tag{25}$$

$$\xi(\mathbf{x},t)|_{t=0} = \mathbf{x} = \mathbf{X}.\tag{26}$$

Note that in the second line of Eqs. (21) and (23), we have made use of the integration-by-parts along with the divergence theorem. Moreover, with the definitions of the test functions given in Eqs. (19) and (20), the boundary terms resulting from the application of the divergence theorem vanish.

# 3 Numerical Examples

We implement the weak form defined in Eqs. (21) to (24) in MOOSE (Multiphysics Object-Oriented Simulation Environment)<sup>[22]</sup>, which is our FEM implementation of choice. MOOSE is an open-source finite element solver package developed primarily at the Idaho National Laboratory that uses PETSc<sup>[23, 24]</sup> for efficient, robust parallelization.

For all the examples shown in this section, we set  $\epsilon = 1 \times 10^{-4}$  and L = 1. Moreover, we choose the material properties, G and  $\kappa$  (corresponding to shear and bulk moduli, respectively, in small strain regime), in such a way that the

(10) 計算工学

resulting behavior resembles that of a rubber-like material with very limited compressibility, more specifically,  $G << \kappa^{[25]}$ . We use Newton-Raphson method as a nonlinear solver, and a standard second order backward difference formula (BDF2) as the time marching algorithm. We utilize the standard linear Lagrange shape functions with the corresponding QUAD4 elements. We also take advantage of the adaptive meshing capabilities in MOOSE for refining the mesh in the phase-field diffuse interface region (see Fig. 3), as well as adaptive time stepping scheme with the initial time step of  $\Delta t = 5 \times 10^{-5} \, s$ .

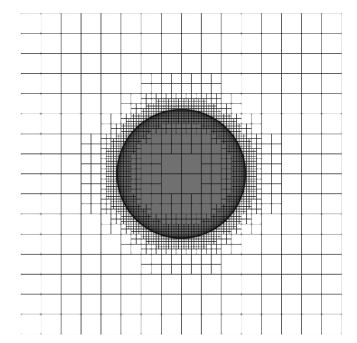


Fig. 3 Adaptive mesh is used to make sure that the diffuse interface is well-resolved without making the entire mesh unnecessarily dense.

#### 3.1 Uniaxial Stretch

In the first set of examples, shown in Fig. 2 and Fig. 3, we use a unit mass density and apply a uniaxial stretch to a bar (represented with the phase-field  $\phi$ ) in two different settings. In the first setting, we fix the bar on one end and apply the stretch to the bar's right side. Figures 4a and 4b show the initial and the deformed configurations, respectively. Numerically, it is straight-forward to fix the bar by letting the bar extend past the left boundary. Note that  $\mathbf{v}_g = \mathbf{0}$  at the boundaries. We then apply the nontrivial stretch condition at the right end of the bar by using a localized uniform velocity field. We observe that, as expected, the bar elongates in the direction of the applied stretch accompanied by thinning in the lateral direction, matching the result of conventional Lagrangian scheme (see Fig. 4b).

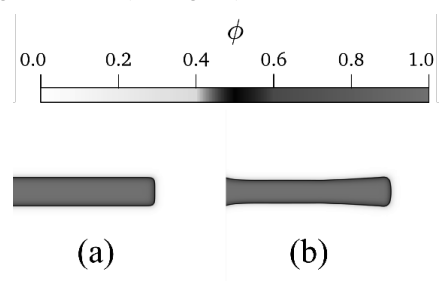


Fig. 4 Deformation of a bar under uniaxial stretch. (a) Is the initial shape and (b) shows the deformed shape. The bar is fixed at the left end while being stretched at the right end using a localized velocity field.

In a second setting, we repeat the uniaxial stretch test in a different scenario. In this case, we take a bar with identical

material properties to the previous example and stretch it from both sides. The stretch is applied equally at both ends of the bar using a localized velocity field. We demonstrate the results of this second uniaxial stretch test in Fig. 5 in which the undeformed and deformed configurations are shown in Fig. 5a and 5b, respectively. We see in Fig. 3b that, matching again the results that MOOSE attains with the regular Lagrangian approach, the elongation of the bar is accompanied by the necking in the middle.

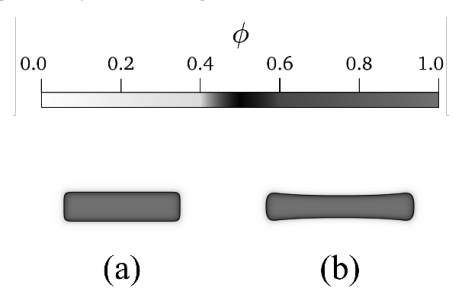


Fig. 5 Deformation of a bar under uniaxial stretch. (a) Is the initial shape and (b) shows the deformed shape. The bar is stretched at both ends using equal localized velocity fields.

# 3.2 Uniform Loading Bending

In this section we report the results from the deflection simulation of a clamped beam subjected to its own weight. The beam is fixed at both ends using the same methodology explained in the previous section. The weight is applied to the beam as a uniform vector field in the vertical direction and enters the balance of linear momentum equation (see Eq. (12)) as  $\rho \mathbf{b}$ , where  $\rho$  is the beam's mass density per unit volume and **b** is the gravity vector field. We use a higher mass density for this example ( $\rho = 10 \text{ kg/m}^3$ ), compared to the previous examples, to create an exaggerated deformation under self-weight. Figure 6a shows the initial undeformed shape and Fig. 6b shows the final deformed shape of the fixed beam. The deformed shape clearly shows the expected behavior of a fixed beam under uniformly distributed load (self-weight), with zero slopes at the fixed ends and in the middle, and maximum deflection in the middle of the beam.

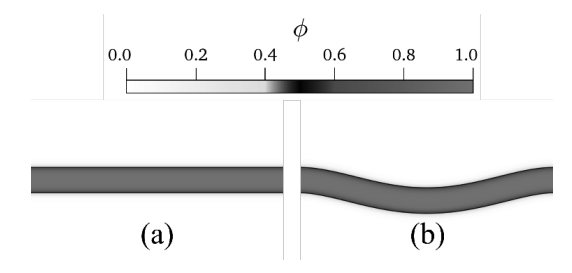


Fig. 6 Deformation of a fixed beam under uniformly distributed load, i.e., self-weight. (a) Is the initial shape and (b) shows the deformed shape.

# 3.3 Advanced Responses I: Stretch and Release This section demonstrates a more dynamic example than

<#1> 特集

the previous ones. Similar to example 2 of section 3.1 (see Fig. 5), we apply two equal and opposite constant velocity fields to the left and the right side of the circle shown in Fig. 7. Furthermore, in order to generate a more dynamic response, we only apply the velocity fields for a limited time from the initial time step ( $t = 0.2 \, s$ ), after which we release the stretched circle by setting the velocities equal to zero. Figure 7 illustrates the process of stretch and release of the circle in time. As expected, after the release (see Fig. 7, second image from the left), the circle gets contracted in the direction that the stretch was applied and eventually relaxes into its initial configuration.

# 3.4 Advanced Responses II: Bouncing Ball

In this final example, we demonstrate the dynamics of the contact of a circular rubber-like solid with the boundary. For this purpose, we simulate a free fall by placing the solid in the middle of the domain and letting gravity be the only force applied to the solid. Note that the velocity is equal to zero at the boundaries. Figure 8 shows the dynamics of the circular solid before, during, and after contact with the boundary.

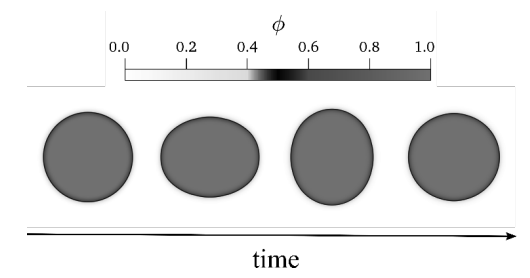


Fig. 7 Deformation of a circular solid domain due to stretch and release. The time increases in the direction of the arrow. From left to right: initial configuration, stretched configuration at *t*=0.2 *s*, contracted shape after the release, and final relaxed configuration.

As expected, the circular solid gains momentum due to gravity and hits the bottom boundary where the velocities are prescribed as zero. It then bounces off the surface after undergoing a large deformation and finally comes to its final stable configuration. One can see from the figure that during this dynamic large deformation simulation, the mass of the circular solid is conserved, and the profile of the phase-field, indicated by the black line, is preserved throughout the evolution in time.

# 4 Conclusions

We have presented a phase-field modified hyper-elastic model in a pure Eulerian framework which integrates the RMT to recover the deformation gradient tensor. We have developed here for the first time the coupled PDEs that govern the balance laws of a phase-field reference map formulation. We then derived the variational form of the equations required for the FEM implementation of the PDEs. We have shown, through several examples, our formulation's

capabilities and potential in different scenarios. We expect this work to contribute to the simulation of complex fluidsolid soft matter ensembles that require physical accuracy and control of the interfaces. In particular, we highlight that the overall mass of the solid during all the examples is conserved. Furthermore, since the material model is nearly incompressible ( $G \ll \kappa$ ), the Jacobian of the deformation J should always stay approximately equal to one, which is also confirmed during our investigation. We would also like to point out that in the dynamic examples shown in sections 3.3 and 3.4, the final relaxed configuration is the configuration at the final time step of our simulations and not the steady-state solution. This is due to the fact that we do not require any dissipation mechanism in our formulations. The dissipation can be introduced, for instance, with the simple addition of a background viscous fluid, which will be a subject of a later study.

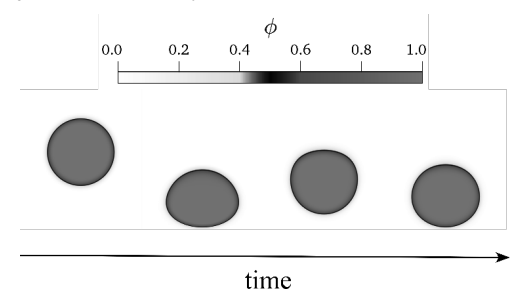


Fig. 8 Deformation of a circular solid domain due to the contact with the surface. The time increases in the direction of the arrow. From left to right: initial configuration, deformation due to the contact with the surface, bouncing off the surface, and final relaxed configuration.

Finally, we note that no special treatment was done to ensure the numerical stability of our solutions. This interesting feature is owing to the fact that we kept the velocity magnitudes of our simulations relatively small to avoid advection dominance. However, the implementation of stabilization methods such as streamline upwind Petrov-Galerkin stabilization method (SUPG) is straightforward and will be explored in the application of this method to more extreme dynamical events.

# References

- [1] Y. Liu, C. Peco, and J. Dolbow, "A fully coupled mixed finite element method for surfactants spreading on thin liquid films," *Comput. Methods Appl. Mech. Eng.*, vol. 345, pp. 429-453, 2019.
- [2] R. Kobayashi, "Modeling and numerical simulations of dendritic crystal growth," *Phys. D Nonlinear Phenom.*, vol. 63, no. 3-4, pp. 410-423, Mar. 1993.
- [3] C. Miehe, M. Hofacker, and F. Welschinger, "A phase field model for rate-independent crack propagation: Robust algorithmic implementation based on operator splits," *Comput. Methods Appl. Mech. Eng.*, vol. 199, no. 45-48, pp. 2765-2778, Nov. 2010.

(12) 計算工学

- [4] F. Greco, L. Filice, C. Peco, and M. Arroyo, "A stabilized formulation with maximum entropy meshfree approximants for viscoplastic flow simulation in metal forming," *Int. J. Mater. Form.*, vol. 8, no. 3, pp. 341-353, 2015.
- [5] B. W. Spencer, W. Jiang, J. E. Dolbow, and C. Peco, "Pellet cladding mechanical interaction modeling using the extended finite element method," *Top Fuel 2016 LWR Fuels with Enhanc. Saf. Perform.*, pp. 929-938, 2016.
- [6] L.-Q. Chen, "Phase-Field Models for Microstructure Evolution," Annu. Rev. Mater. Res., vol. 32, no. 1, pp. 113-140, Aug. 2002.
- [7] A. Rosolen, C. Peco, and M. Arroyo, "An adaptive meshfree method for phase-field models of biomembranes. Part I: Approximation with maximum-entropy basis functions," *J. Comput. Phys.*, vol. 249, pp. 303-319, Sep. 2013.
- [8] C. Peco, A. Rosolen, and M. Arroyo, "An adaptive meshfree method for phase-field models of biomembranes. Part II: A Lagrangian approach for membranes in viscous fluids," *J. Comput. Phys.*, vol. 249, pp. 320-336, Sep. 2013.
- [9] B. Li, C. Peco, D. Millán, I. Arias, and M. Arroyo, "Phase-field modeling and simulation of fracture in brittle materials with strongly anisotropic surface energy," *Int. J. Numer. Methods Eng.*, vol. 102, no. 3-4, pp. 711-727, 2015.
- [10] C. Peco, W. Chen, Y. Liu, M. M. Bandi, J. E. Dolbow, and E. Fried, "Influence of surface tension in the surfactant-driven fracture of closely-packed particulate monolayers," *Soft Matter*, vol. 13, no. 35, pp. 5832-5841, 2017.
- [11] C. Peco, Y. Liu, C. Rhea, and J. E. Dolbow, "Models and simulations of surfactant-driven fracture in particle rafts," *Int. J. Solids Struct.*, vol. 156-157, pp. 194-209, 2019.
- [12] J. Xu, G. Vilanova, and H. Gomez, "A Mathematical Model Coupling Tumor Growth and Angiogenesis," *PLoS One*, vol. 11, no. 2, p. e0149422, Feb. 2016.
- [13] M. Fritz, P. K. Jha, T. Köppl, J. T. Oden, and B. Wohlmuth, "Analysis of a new multispecies tumor growth model coupling 3D phase-fields with a 1D vascular network," *Nonlinear Anal. Real World Appl.*, vol. 61, p. 103331, Jun. 2020.
- [14] X. Kuang *et al.*, "Computable early Caenorhabditis elegans embryo with a phase field model," *PLOS Comput. Biol.*, vol. 18, no. 1, p. e1009755, Jan. 2022.

- [15] F. Ghanbari, F. Costanzo, D. P. Hughes, and C. Peco, "Phase-field modeling of constrained interactive fungal networks," *J. Mech. Phys. Solids*, vol. 145, p. 104160, Dec. 2020.
- [16] N. Takashi and T. J. R. Hughes, "An arbitrary Lagrangian-Eulerian finite element method for interaction of fluid and a rigid body," *Comput. Methods Appl. Mech. Eng.*, vol. 95, no. 1, pp. 115-138, Feb. 1992.
- [17] T. Shimada, K. Nishiguchi, C. Peco, S. Okazawa, and M. Tsubokura, "Eulerian unified formulation for fluid-structure interaction problems using marker particles with Reference map," *Trans. Japan Soc. Comput. Eng. Sci.*, vol. 2022, p. 20220002, 2022.
- [18] K. Kamrin and J.-C. Nave, "An Eulerian approach to the simulation of deformable solids: Application to finite-strain elasticity," Jan. 2009.
- [19] C. H. Rycroft, C. H. Wu, Y. Yu, and K. Kamrin, "Reference map technique for incompressible fluid-structure interaction," *J. Fluid Mech.*, vol. 898, p. A9, 2020.
- [20] T. Shimada, K. Nishiguchi, C. Peco, S. Okazawa, and M. Tsubokura, "Eulerian formulation using lagrangian marker particles with reference map technique for fluid-structure interaction problem," in 9th edition of the International Conference on Computational Methods for Coupled Problems in Science and Engineering, 2021, pp. 1-7.
- [21] B. Valkov, C. H. Rycroft, and K. Kamrin, "Eulerian method for multiphase interactions of soft solid bodies in fluids," *J. Appl. Mech. Trans. ASME*, vol. 82, no. 4, Sep. 2014.
- [22] A. D. Lindsay *et al.*, "2.0 MOOSE: Enabling massively parallel multiphysics simulation," *SoftwareX*, vol. 20, p. 101202, Dec. 2022.
- [23] J. Zhang et al., "The PetscSF Scalable Communication Layer," IEEE Trans. Parallel Distrib. Syst., vol. 33, no. 4, pp. 842-853, Eeb. 2021
- [24] S. Balay, W. D. Gropp, L. C. McInnes, and B. F. Smith, "Efficient Management of Parallelism in Object-Oriented Numerical Software Libraries," in *Modern Software Tools for Scientific Computing*, Boston, MA: Birkhäuser Boston, 1997, pp. 163-202.
- [25] A. F. Bower, "Applied mechanics of solids," Appl. Mech. Solids, pp. 1-795, Jan. 2009.